

# ADVANCED MATERIALS

## Supporting Information

for *Adv. Mater.*, DOI: 10.1002/adma.202106607

Self-Assembly of Oriented Antibody-Decorated Metal–Organic Framework Nanocrystals for Active-Targeting Applications

*Karen Alt,\* Francesco Carraro, Edwina Jap, Mercedes Linares-Moreau, Raffaele Riccò, Marcello Righetto, Marco Bogar, Heinz Amenitsch, Rania A. Hashad, Christian Doonan, Christoph E. Hagemeyer,\* and Paolo Falcaro\**

# Supporting Information

## Self-Assembly of Oriented Antibody-Decorated Metal-Organic Framework Nanocrystals for Active-Targeting Applications

*Karen Alt,\* Francesco Carraro, Edwina Jap, Mercedes Linares-Moreau, Raffaele Riccò, Marcello Righetto, Marco Bogar, Heinz Amenitsch, Rania A. Hashad, Christian Doonan, Christoph E. Hagemeyer,\* and Paolo Falcaro\**

### **CONTENTS**

#### **Experimental Section**

##### **Tables**

Table S1: SAXS fit parameters

##### **Figures**

Figure S1: Kinetics of the nucleation and growth of ZIF-C\* $\alpha$ -HER2 over a time frame of 30 min.

Figure S2: XRD data of ZIF-C and ZIF-C\*Ab (Ab = hIgG or  $\alpha$ -HER2)

Figure S3: FTIR data of Ab, ZIF-C and ZIF-C\*Ab (Ab = hIgG or  $\alpha$ -HER2); ZIF-C crystal structure.

Figure S4: Immobilization efficiency of ZIF-C\* $\alpha$ -HER2 and QD@ZIF-C\* $\alpha$ -HER2

Figure S5: SEM images of ZIF-C\*Ab (Ab = hIgG or  $\alpha$ -HER2)

Figure S6: TEM images of ZIF-C\* $\alpha$ -HER2

Figure S7: SAXS Stopped-flow setup

Figure S8: Time-resolved SAXS data of ZIF-C\* $\alpha$ -HER2

Figure S9: SAXS data of ZIF-C\* $\alpha$ -HER2

Figure S10: Time-resolved SAXS data of bare ZIF-C

Figure S11: Schematic representations of the different Ab components

Figure S12: Time-resolved SAXS data of ZIF-C + Fc

Figure S13: Time-resolved SAXS data of ZIF-C + Fab

Figure S14: Time-resolved SAXS data of ZIF-C + F(ab')<sub>2</sub>

Figure S15: Time-resolved SAXS data of ZIF-C + SGP

Figure S16: Time-resolved SAXS data of ZIF-C + SG

Figure S17: XRD data of pyrolyzed ZIF-C\* $\alpha$ -HER2 and ZIF-C\*IgG

Figure S18: SEM images of pyrolyzed ZIF-C\* $\alpha$ -HER2

Figure S19: AFM images of pyrolyzed ZIF-C\* $\alpha$ -HER2

Figure S20: AFM analysis of pyrolyzed ZIF-C\* $\alpha$ -HER2 with layer thickness estimation

Figure S21: AFM analysis of pyrolyzed ZIF-C\* $\alpha$ -HER2 with hole size estimation

Figure S22: Cellular internalization of ZIF-C\* $\alpha$ -fHER2 (2D)

Figure S23: Cellular internalization of ZIF-C\* $\alpha$ -fHER2 (3D)

Figure S24: FTIR and XRD data of ZIF-C\*hIgG and QD@ ZIF-C\* $\alpha$ -HER2

Figure S25: TEM images of QD@ZIF-C\* $\alpha$ -HER2

Figure S26: SEM and EDX data of QD@ ZIF-C\* $\alpha$ -HER2

## **Experimental Section**

### ***Materials***

All chemicals were purchased from Sigma-Aldrich unless otherwise noted. Cancer cell lines were obtained from the American Type Culture Collection unless otherwise stated. Cell culture media and media components were purchased from Gibco unless otherwise stated. Monoclonal antibodies (Abs) anti-HER2 ( $\alpha$ -HER2) (Trastuzumab, Roche, Switzerland) were purchased from the Alfred Health Pharmacy (Alfred Hospital, Melbourne, Australia). Human IgG (hIgG) was purchased from Sigma. Purified fragments of hIgG (Bethyl Laboratories Inc., USA) were used as non-binding control. Antigen fragments (Fab; P80-215, 1 mg mL<sup>-1</sup>), F(ab')<sub>2</sub> (P80-130, 1 mg mL<sup>-1</sup>), and fragment crystallizable (Fc; P80-204, 1 mg mL<sup>-1</sup>) were purchased from Sanova Pharma GmbH (Austria). Sialylglycan (SG,  $\alpha$ -2,6; Fushimi, Japan) was purchased from Wako Chemical GmbH (Germany). Sialylglycopeptide (SGP,  $\alpha$ -2,6; Peptide Institute Inc., Japan) was purchased from PeptaNova GmbH (Germany). All reagents were used as received.

### ***Experimental procedures***

#### **Synthesis of metal-organic framework (MOF) biocomposites**

In a typical synthesis, the Ab (50  $\mu$ g) was added to 240 mM 2-methylimidazole (HmIM; 33.5  $\mu$ L) and then incubated in a 30 mM Zn<sup>2+</sup> solution (zinc acetate dihydrate; 66.5  $\mu$ L) at 37 °C for 20 min. These solutions were prepared using 10 mM 3-(*N*-morpholino)propanesulfonic acid (MOPS) buffer pH 7.1. Following incubation, the MOF\*Ab biocomposite (MOF = zeolitic imidazolate framework ZIF-C) was washed twice with MOPS buffer pH 7.1 in a final volume of 200  $\mu$ L by centrifugation for 30 s at 1000g and finally resuspended in buffer with a final Ab concentration of 500  $\mu$ g mL<sup>-1</sup>.

For the synthesis of quantum dot (QD)-containing biocomposites (QD@ZIF-C\*Ab), an 8  $\mu$ M QD suspension (1  $\mu$ L; 625 nm – carboxyl QDs, Thermo Fisher Scientific, USA) was added to the HmIM solution prior to mixing with the Zn<sup>2+</sup> solution.

#### **MOF growth kinetics**

Evaluation of the MOF growth kinetics by monitoring changes in the optical density of the MOF solution was performed using a FLUOstar OPTIMA microplate reader (BMG Labtech, Germany) equipped with two built-in reagent injectors. The injection pumps were filled with the following buffers: 240 mM HmIM (pump 1) and 30 mM Zn<sup>2+</sup> (pump 2); 31 cycles and 60 s per cycle were applied. The Ab samples in 10 mM MOPS buffer pH 7.1 were placed in a 96-well plate and 240 mM HmIM (33.5  $\mu$ L) was added in cycle 1, followed by the addition of 30 mM of Zn<sup>2+</sup> (66.5  $\mu$ L) in cycle 3. The increase in the optical density was measured and correlated with MOF growth.

#### **Encapsulation efficiency**

Following self-assembly of the biocomposites, the supernatant was retrieved to determine the amount of Ab using a bicinchoninic acid assay (Thermo Fisher Scientific, USA). The assay was performed according to the manufacturer's protocol.

## Fluorescence labeling of Abs

Abs ( $\alpha$ -HER2 or hIgG) were fluorescently labelled using an *N*-hydroxysuccinimide ester-activated Alexa Fluor 488 (A1488) dye (Invitrogen™, Germany) following the manufacturer's protocol. Briefly, the Ab (1 molar equivalent) was incubated with A1488 (10 molar equivalents) at pH 7.5 and 4 °C for 3 h. The fluorescently labeled Ab (fAb) was purified using a 10k centrifugation column (Amicon, USA).

## Cell culture

The HER2-receptor-positive (HER2-R+) cell lines SKOV-3 and HER2-receptor-negative (HER2-R-) cell line MDA-MB-231 were grown in RPMI 1640 medium with 10% fetal bovine serum (Sigma, USA) and 1% penicillin (10,000 units mL<sup>-1</sup>)/streptomycin (10,000  $\mu$ g mL<sup>-1</sup>) at 37 °C in a humidified atmosphere of 5% CO<sub>2</sub>. Subcultures were prepared every 2–3 days to maintain exponential growth.

## Binding studies

To evaluate the binding capability of the QD@ZIF-C\*Ab biocomposites via flow cytometry (CytoFlex & Canto, Beckman Coulter, USA), the biocomposites were first prepared as follows.  $\alpha$ -fHER2 (50  $\mu$ g) or control fhIgG (50  $\mu$ g) ( $\lambda_{\text{Ex}}/\lambda_{\text{Em}}$ : 495/519 nm) was incubated with 240 mM HmIM (33.5  $\mu$ L), 8  $\mu$ M QD solution (1  $\mu$ L,  $\lambda_{\text{Ex}}/\lambda_{\text{Em}}$ : 405/625 nm; Invitrogen, USA), and 30 mM Zn<sup>2+</sup> solution (66.5  $\mu$ L) at 37 °C for 20 min. Post incubation, the biocomposites were washed twice with 10 mM MOPS buffer pH 7.1 in a final volume of 200  $\mu$ L by centrifugation for 30 s at 1000g and finally resuspended in buffer with a final concentration of 500  $\mu$ g mL<sup>-1</sup>.

Then, cells were freshly harvested from the tissue culture flasks and a single-cell suspension prepared in phosphate-buffered saline with 3% Fetal Calf Serum and 0.5 mM ethylenediaminetetraacetic acid. Specifically,  $2 \times 10^5$  cells were incubated with 2.5  $\mu$ g mL<sup>-1</sup> of the biocomposites at room temperature and after washing, the relative fluorescence of the stained cells was measured using either BD FACSCanto™ II or CytoFLEX flow cytometer and analyzed using BD FACSDiva (Becton Dickinson, USA) or CytExpert (Beckman Coulter, USA) software. Post-data acquisition analysis was performed using FlowJo (Version 10, FlowJo LLC, USA).

## Confocal microscopy

To assess cell internalization,  $1.25 \times 10^4$  cells per well were treated with 2.5  $\mu$ g mL<sup>-1</sup> of either ZIF-C\* $\alpha$ -fHER2 or ZIF-C\*fhIgG and nuclear stain 4',6-diamidino-2-phenylindole at 1  $\mu$ g mL<sup>-1</sup> for 20 min at 37 °C. After incubation, the cells were washed several times and transferred to a CELLview™ cell culture slide (Greiner AG, Austria). One cohort was additionally stained with 4  $\mu$ g mL<sup>-1</sup> cell membrane dye Wheat germ agglutinin, Alexa Fluor™ 647 conjugate (Invitrogen/Thermo Fisher, USA). Confocal images and *z*-stacks were acquired using a Nikon A1r confocal microscope with a 40 $\times$  objective and a 4 $\times$  scanner zoom. Lasers (405 and 488 nm) were used for excitation, and emission was detected using 450/50 nm and 535/50 nm filters. Quantification of the cell binding and internalization of the ZIF-C\*Ab biocomposites was performed using Fiji software.<sup>[1]</sup> Region of interests (ROIs) were drawn around the outline of the bright-field cells in focus and analyzed through the stacks to ensure that the ROIs covered cells throughout the stack. An ROI was then added to the ROI manager and applied to 500–550 nm channel images. To simultaneously measure the A1488 signal in all ROIs on every slice, the multi-

measure function was used to measure the integrated density, where measurement was limited to the threshold value. Data are expressed as integrated density per cell.

### **Statistical analysis**

All quantitative data are reported as means  $\pm$  standard deviations. Statistical analysis was performed using ANOVA followed by a multiple comparison test with  $p < 0.05$  considered as statistically significant (Prism 7, GraphPad).

### ***Characterization techniques***

#### **X-ray diffraction (XRD)**

XRD patterns were acquired using a SmartLab II Rigaku X-ray diffractometer equipped with a Cu anode ( $\lambda = 1.5406 \text{ \AA}$ ) and operating at 9 kW. Prior to analysis, the biocomposites were washed three times by centrifugation (30 s, 1000g) with deionized water, the supernatant was discarded, and the products were dried at ambient pressure and temperature overnight.

#### **Scanning electron microscopy (SEM)**

SEM images were captured using a Tescan VEGA 3 scanning electron microscope equipped with a tungsten source filament operating at 20 kV. Prior to analysis, the biocomposites were washed three times by centrifugation (30 s, 1000g) with deionized water, the supernatant was discarded, and the products were dried at ambient pressure and temperature overnight. The powder samples were then sputter-coated with gold. Energy-dispersive X-ray spectroscopy (EDX) analysis were conducted using the same instrument.

#### **Attenuated total reflectance–Fourier transform infrared (ATR-FTIR) spectroscopy**

FTIR spectra were recorded on a Bruker ALPHA spectrometer fitted with an ATR accessory with a diamond window in the range of 500–4000  $\text{cm}^{-1}$ . Prior to analysis, the biocomposites were washed three times by centrifugation (30 s, 1000g) with deionized water, the supernatant was discarded, and the products were dried at ambient pressure and temperature overnight.

#### **Transmission electron microscopy (TEM)**

TEM images were captured on a JEM-1400 flash electron microscope operating at 100 kV. Samples were dispersed in deionized water by thorough vortex stirring and sonication. An aliquot (20  $\mu\text{L}$ ) of the dispersion was drop-cast on an ultrathin ( $\sim 3 \text{ nm}$ ) continuous carbon film-coated holey carbon on a copper grid (Latech) and dried overnight

#### **Atomic force microscopy (AFM)**

AFM measurements were performed using an Asylum Research Cypher ES atomic force microscope (Oxford Instruments) in tapping mode using blueDrive photothermal excitation. The images were acquired in air, at room temperature and at a scanning rate of 2 Hz, using Oxford Instruments HQ75 silicon probes.

#### **Time-resolved small-angle X-ray scattering (SAXS)**

Time-resolved SAXS data were collected on the SAXS beamline at the ELETTRA synchrotron light source.<sup>[2]</sup> The experiments were conducted at a photon energy of 8 keV, covering the range of

momentum transfer  $q$  (where  $q = 4\pi \sin(\theta/2)/\lambda$ ) between 0.07 and 5 nm<sup>-1</sup> at the scattering angle  $\theta$  and wavelength  $\lambda$ . The nucleation and growth kinetics of the MOFs were monitored using a commercial stopped-flow apparatus SFM-4 (Bio-Logic, France) modified for synchrotron radiation SAXS investigations (Figure S7). Two independently stepper-motor-driven syringes were filled respectively with the Zn<sup>2+</sup> solution and HmIM solution (or a mixture of HmIM and  $\alpha$ -HER2 or  $\alpha$ -HER2 fragments). Fixed volumes of both solutions were injected at a flow rate of several milliliters per second first into a mixer and subsequently into a quartz capillary (1.5 mm diameter) placed in the X-ray beam (the mixing/injection process lasts a few milliseconds). The start of the mixing sequence is triggered from the X-ray data-acquisition system, which captured images with a time resolution of 100 ms (detector: Pilatus3 1M, Dectris Ltd., Switzerland; sample-to-detector distance: 1260 mm, as determined with a silver behenate calibration sample). The volume ratio between the two solutions was set accordingly to maintain the conditions used for the syntheses in all batches. All the experiments were performed at room temperature. The SAXS pattern of Zn<sup>2+</sup> in buffer solution was measured to assess and subtract the instrument background signal from the data. The resulting two-dimensional images were azimuthally integrated to obtain a one-dimensional pattern of normalized intensity (corrected for transmission and intensity fluctuations) versus scattering vector  $q$ .

### SAXS Data evaluation

Data analysis was carried out with the software package Igor Pro (IGOR Pro 7.0.8.1, Wavemetrics, USA). The Porod-invariant was estimated as follows:  $Q = \int_{q_1}^{q_2} I(q) q^2 dq$  [3] within the  $q$ -region, in which the larger variations were observed, i.e.  $q_1 = 0.087$  and  $q_2 = 0.406 \text{ nm}^{-1}$ . An increasing trend of this quantity describes the formation of agglomerates, whereas a plateau points toward stable conditions within the dimensional window defined by the extremes of the  $q$ -integration.

Various models were applied to interpret the scattering of the samples. Generally, for hierarchical structures, the SAXS signal can be expressed as:

$$I(q) = B + \frac{c}{q^p} + A P(q) S(q)$$

in which the residual background given by the incoherent contributions of the solvents is defined by a constant  $B$  together with an (optional) power law (constant  $c$  and exponent  $p$ ), which describes diffuse scattering from aggregates larger than the resolution limit of the experiment. The scattering of the aggregates formed during the synthesis is given by the product of a form factor  $P(q)$  and a structure factor  $S(q)$ . The term  $P(q)$  takes into account the shape and size of the particles, whereas the term  $S(q)$  defines particle correlation/ordering. The scaling factor  $A$  represents the contribution of contrast and concentration of the particles.

Here, for the structure factor  $S(q)$ , two models were used: a sticky hard sphere (SHS) model<sup>[4,5]</sup> and a simplified model consisting of a single peak due to near-range order.<sup>[6]</sup> The first model  $S_{\text{SHS}}(q)$  was used in most cases, in which particles grow into a spherical shape. Furthermore, the minimum inter-particle distance  $D_{\text{SHS}}$ , the depth  $\varepsilon$ , and the relative extension  $\lambda$  of the attractive potential well were determined from the structure factor.

For the second simplified model, which was used to quantify a disordered near-range particle correlation, the structure factor  $S_{\text{ord}}(q)$  was applied and described as:

$$S_{\text{ord}}(q) = 1 + \alpha_V K(w_V(q - q_V), s_V)$$

where  $K(x,s)$  is the Voigt function for the peak shape and the Voigt peak parameters  $\alpha_V$ ,  $w_V$ ,  $q_V$ , and  $s_V$  are the peak amplitude, peak position, half-width at half-maximum, and peak shape factor, respectively. The average inter-particle distance  $\langle d \rangle$  can be calculated from the peak position  $q_V$ :  $\langle d \rangle = 2\pi/q_V$ .

As for the form factor  $P(q)$ , different models were used, as detailed below:

- A simplified model for spheres with a large size distribution, which was approximated with the Debye–Anderson–Brumberger model<sup>[7]</sup> (DAB model),  $P(q) = \frac{1}{(1+\xi^2 q^2)^2}$  where  $\xi$  is the correlation parameter. By comparison with the Guinier approximation for spherical particles,  $\xi$  can be related to a spherical particle with radius  $R$  where  $R = \sqrt{10}\xi$ .
- A simple empirical rod model similar to the DAB model with the adjustment of the asymptotic behavior for  $q \ll 1/\xi$  and  $q \gg 1/\xi$  (rod model), expressed as  $P(q) = \frac{1}{q(1+\xi^2 q^2 + \varepsilon^3 q^3)}$  where  $\xi$  is the correlation parameter and  $\varepsilon$  is related to the surface-to-volume ratio. By comparison with the Guinier approximation for quasi infinite rods,  $\xi$  can be related to a rod with cross-sectional radius expressed as  $R_c = 2\xi$ .
- A simplified model for quasi infinite large plates with a thickness  $T$  (plate model), which is based on the Cauchy integral<sup>[7]</sup> and the asymptotic behavior of the scattering for the  $q$ -range  $q \ll 1/\xi$  for plates with lateral size larger than thickness, expressed as  $P(q) = \frac{1}{(1+\xi^2 q^2)q^2}$  where  $\xi$  is the thickness correlation parameter. By comparison with the Guinier approximation for quasi infinite plates,  $\xi$  can be related to a plate with thickness  $T$  where  $T = \sqrt{12}\xi$ .
- Polydisperse spherical particles with Schulz distribution for their sizes (spheres ScS model); the form factor describes a set of spheres following Schulz distribution for the number size distribution,<sup>[8,9]</sup>  $P(q) = |F_{ScS}(q, R, \sigma)|^2$  where  $F_{ScS}$  is the scattering amplitude of the spheres following the Schulz distribution,  $R$  is the average particle radius and  $\sigma$  is the standard deviation.

Table S1 summarizes the samples analyzed and the corresponding model used for data fitting.

## Tables

**Table S1.** Summary of SAXS models applied for the samples and reference to the corresponding supporting figures

Sample	$P(q)$	$S(Q)$	Corresponding figure
ZIF-C* $\alpha$ -HER2	DAB model (time < 3.7 s)	$S_{\text{ord}}(q)$	Figure S8
	Plate model (time > 3.7 s)		
Bare MOF	Spheres ScS	1	Figure S10
ZIF-C + Fc region	Plate model (time < 5 s)	1	Figure S12
	Plate model (time > 5 s)	$S_{\text{ord}}(q)$	
ZIF-C + Fab region	Spheres ScS	1	Figure S13
ZIF-C + F(ab') <sub>2</sub> region	Spheres ScS (time < 6.2 s)	$S_{\text{SHS}}(q)$	Figure S14
	Rod model (time > 6.2 s)	1	
ZIF-C + SGP	Hierarchical spheres ScS	1	Figure S15
ZIF-C + SG	Hierarchical spheres ScS	1	Figure S16
Dry powder of ZIF-C* $\alpha$ -HER2	Hierarchical spheres ScS	$S_{\text{SHS}}(q)$	Figure S9

## Figures

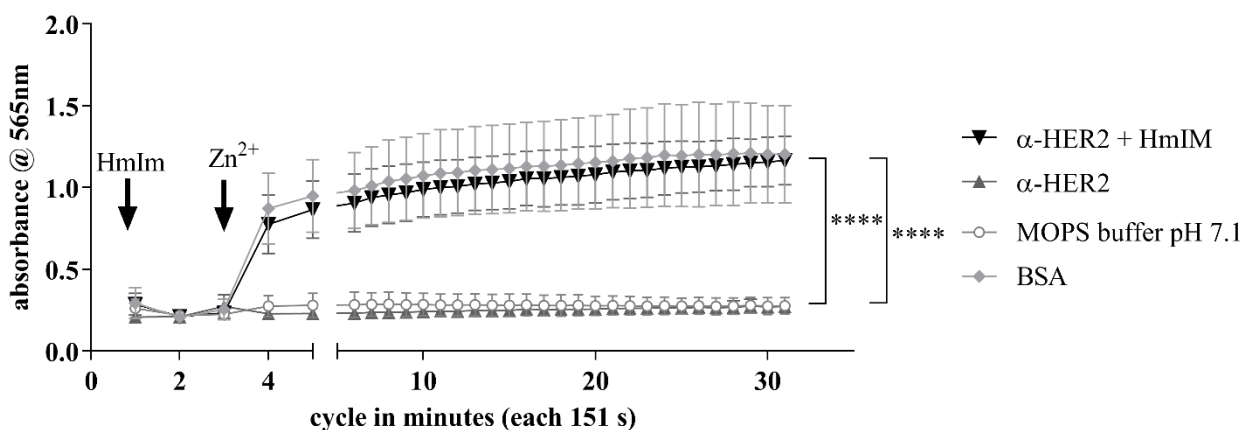


**Figure S1.** Kinetics of the formation of ZIF-C\* $\alpha$ -HER2 over a time frame of 30 min monitored with UV-Vis Spectroscopy ( $\lambda=565$  nm). Bovine serum albumin (BSA) was used as a control as it is a model protein that induces biomimetic mineralization of ZIF (from  $\text{Zn}^{2+}$  and HmIM in water). Statistical analysis was performed using ANOVA followed by a multiple comparison test ( $\pm$  s.e.m.) ( $n = 5$ ); with \*\*\*\*  $p < 0.0001$  considered as statistically significant.

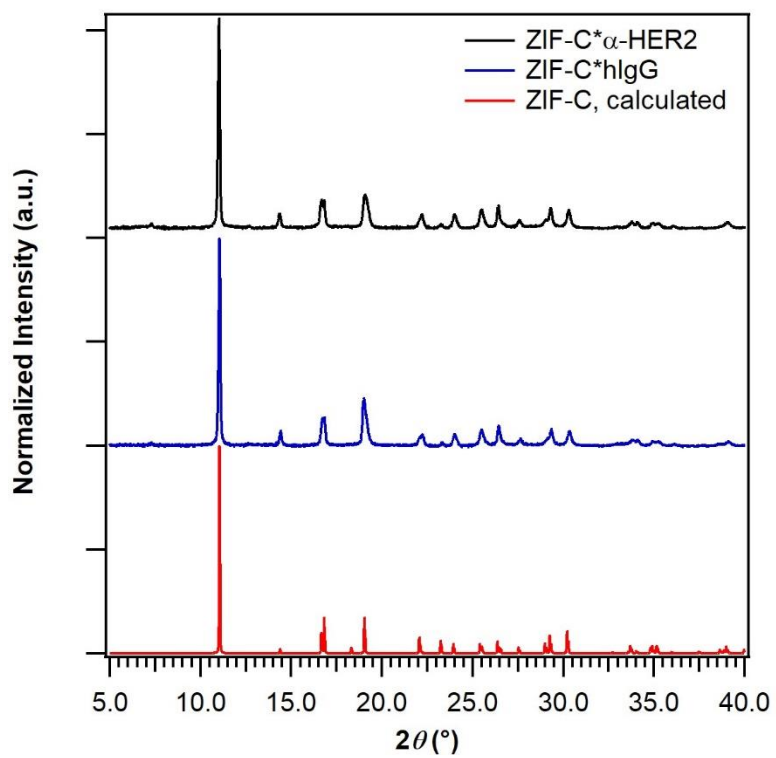


**Figure S2.** Calculated XRD pattern of ZIF-C and experimental XRD patterns of ZIF-C\*  $\alpha$ -HER2 and ZIF-C\*hIgG biocomposites.

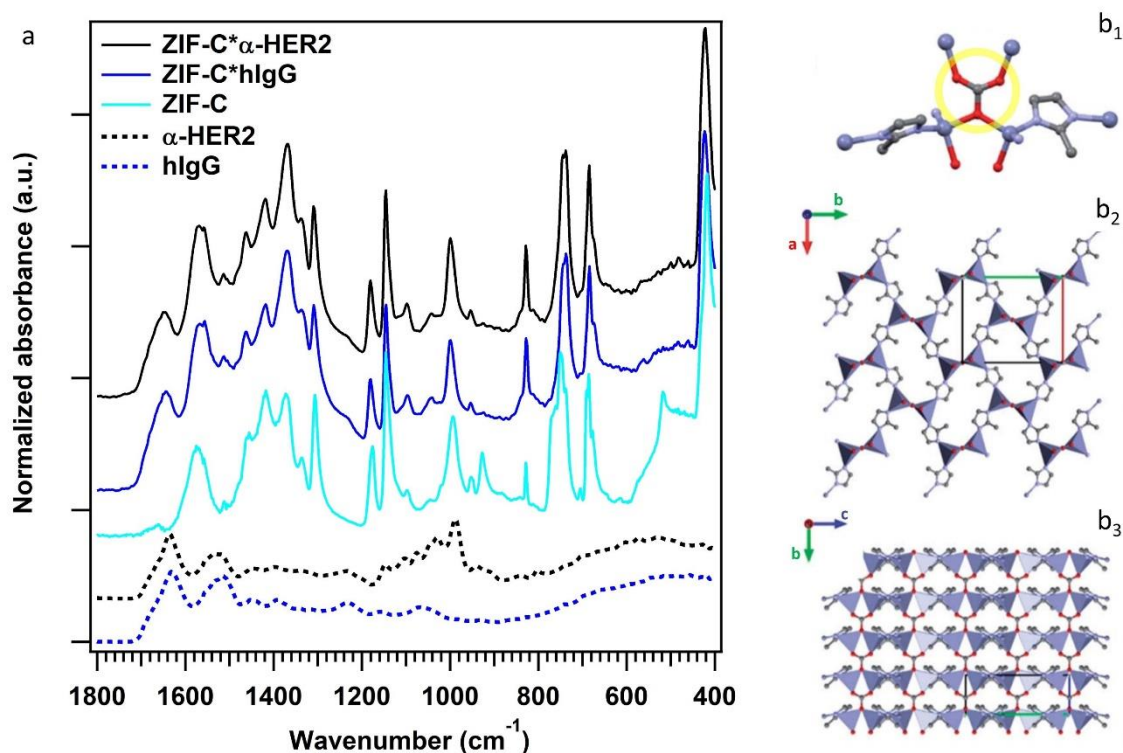


**Figure S3.** FTIR spectra of Abs  $\alpha$ -HER2 and hIgG and biocomposites ZIF-C\* $\alpha$ -HER2, ZIF-C\*hIgG and pure ZIF-C. The spectrum of ZIF-C,  $\text{Zn}_2(\text{mIM})_2(\text{CO}_3)$ , and the related biocomposite shows bands in the 700–850 and 1300–1600  $\text{cm}^{-1}$  regions that can be assigned to bending ( $828 \text{ cm}^{-1}$ ) and asymmetric stretching modes ( $1575$  and  $1375 \text{ cm}^{-1}$ ) of  $\text{CO}_3^{2-}$ . The Zn–N stretching mode, typically at  $420 \text{ cm}^{-1}$  for *sod* or *dia* ZIF-8,  $\text{Zn}(\text{mIM})_2$ , for ZIF-C is centred at  $425 \text{ cm}^{-1}$  because of the coordination of  $\text{CO}_3^{2-}$  with Zn and the related change in coordination environment. b1) coordination mode of Zn with  $\text{CO}_3^{2-}$  highlighted in yellow; b2) crystalline framework of ZIF-C viewed along the c axis; b3) crystalline framework of ZIF-C viewed along the a axis. The Zn, O, N and C atoms are shown in blue, red, light blue and grey, respectively. Schemes in b1, b2, and b3 are adapted from F. Carraro, M. de J. Velasquez-Hernandez, E. Astria, W. Liang, L. Twight, C. Parise, M. Ge, Z. Huang, R. Ricco, X. Zou, L. Villanova, C. O. Kappe, C. J Doonan, P. Falcaro. *Chemical Science* 2020, 11, 3397-3404. <https://doi.org/10.1039/C9SC05433B>

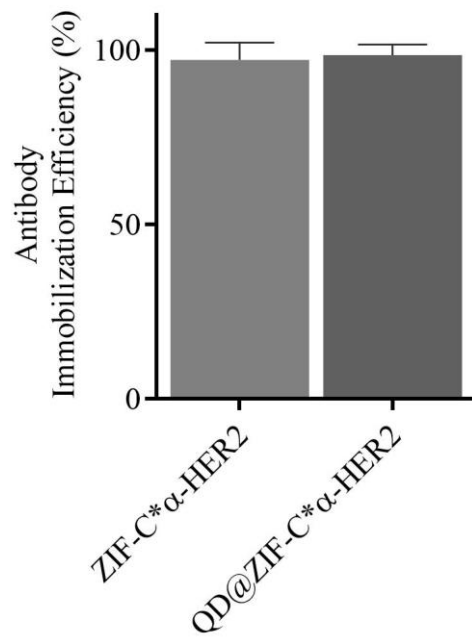


**Figure S4.** Antibody immobilization efficiency of ZIF-C\*α-HER2 and QD@ZIF-C\*α-HER2 ( $n = 3$ ).

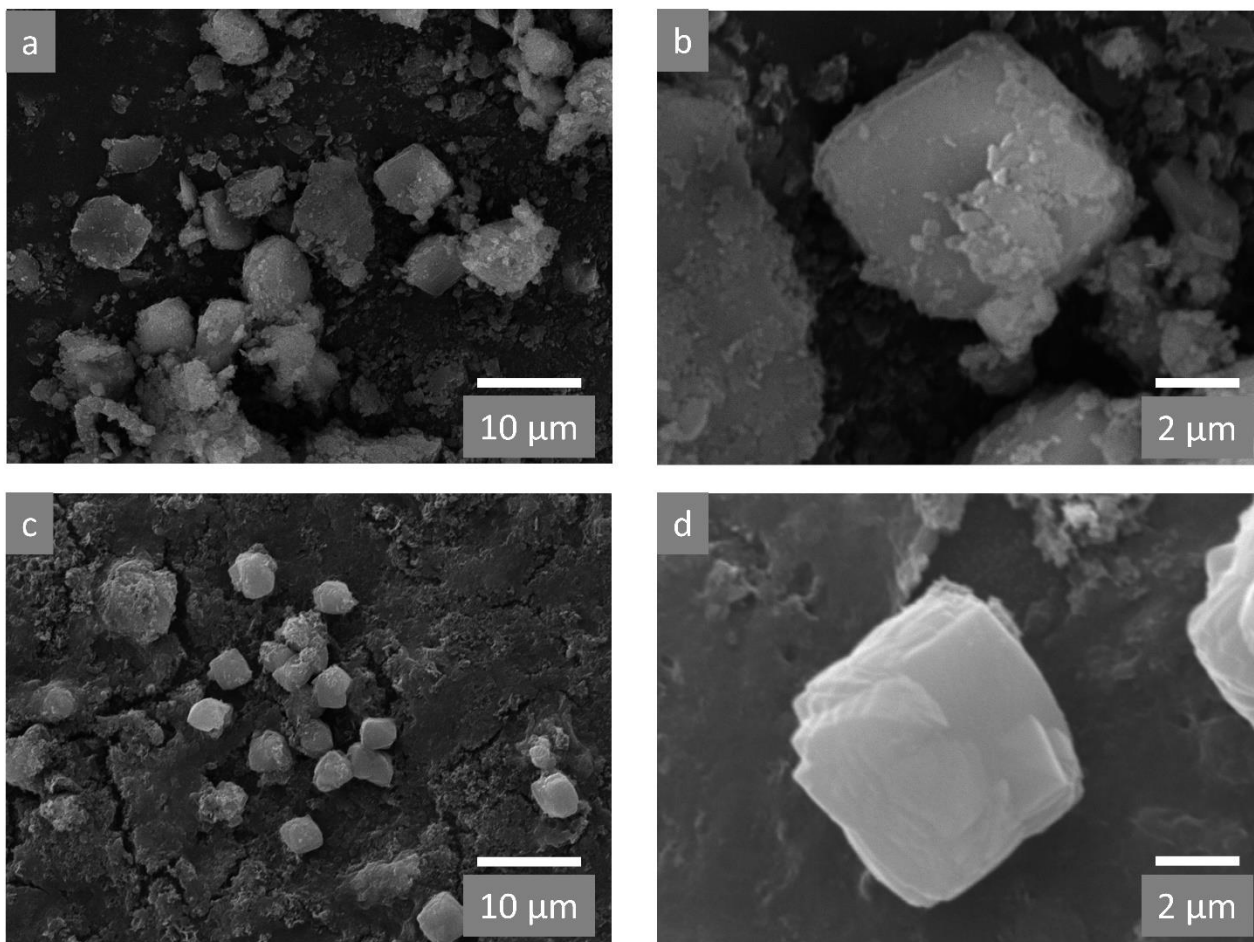


**Figure S5.** Low- and high-magnification SEM images of (a, b) ZIF-C\*α-HER2 and (c, d) ZIF-C\*hIgG biocomposites.

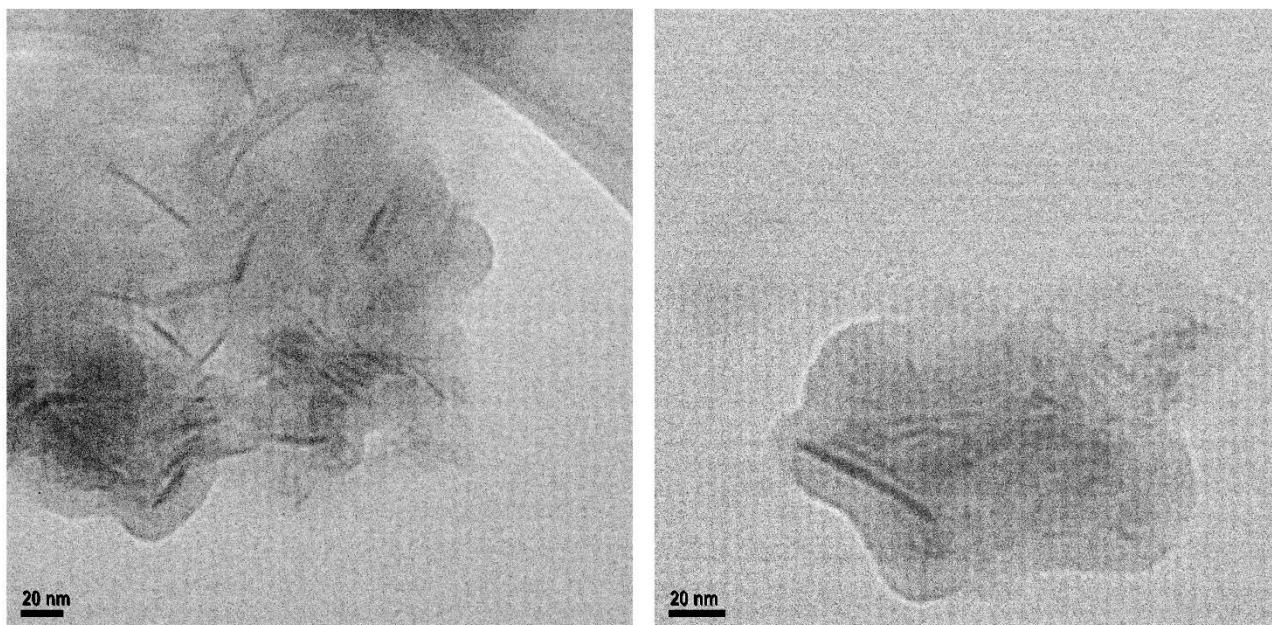


**Figure S6.** TEM images of ZIF-C\* $\alpha$ -HER2 at different magnifications.

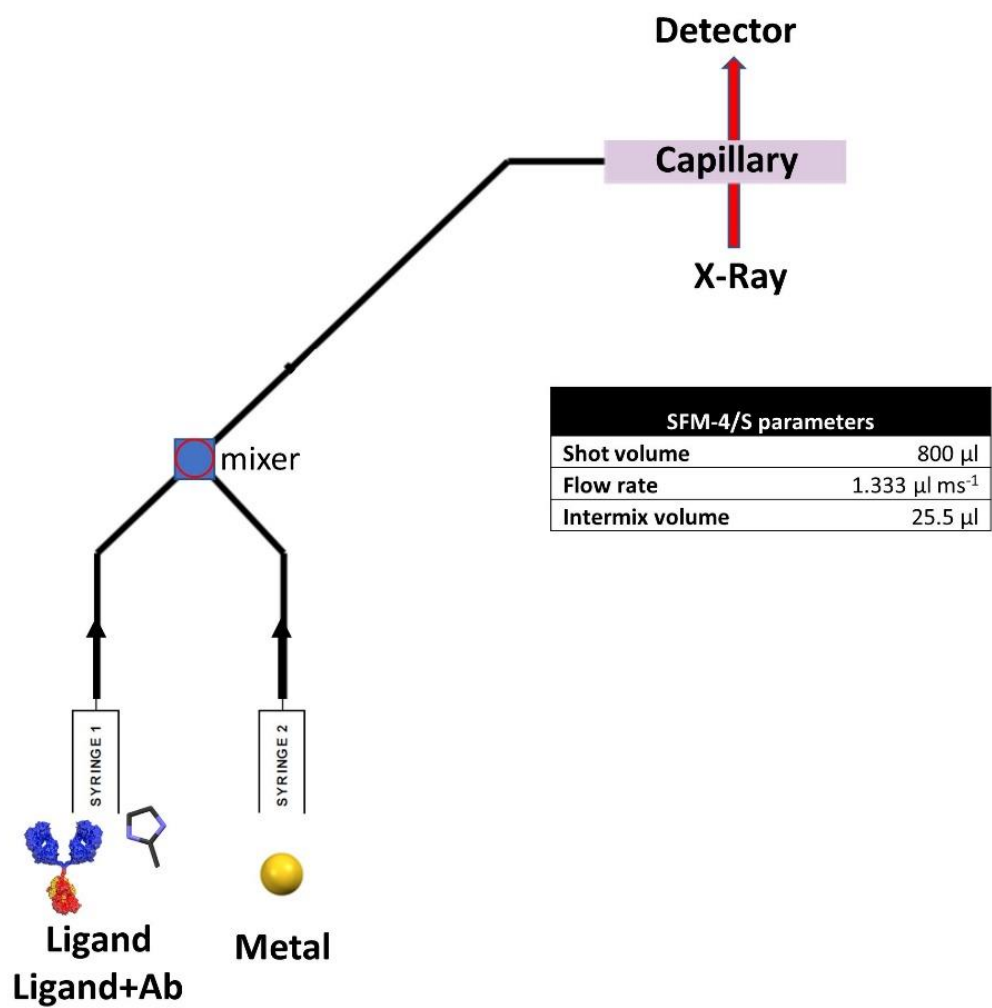


**Figure S7.** Schematic of the stopped-flow setup used for the SAXS measurements.

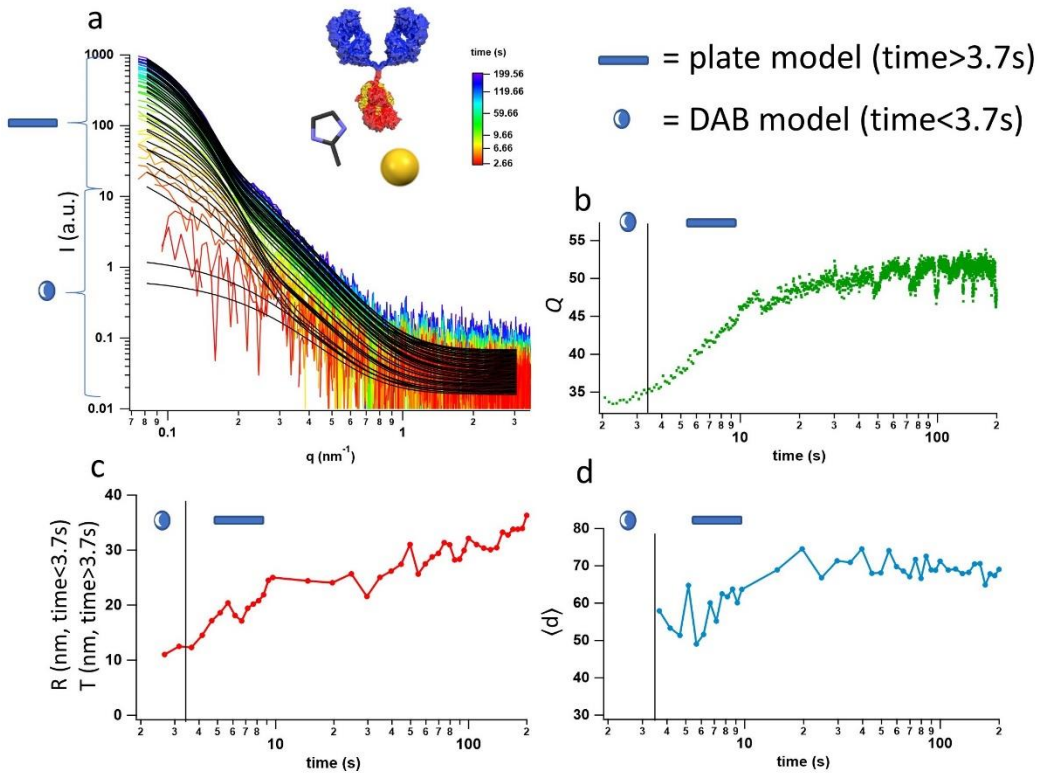


**Figure S8.** (a) Time-resolved SAXS patterns recorded during the growth of ZIF-C\* $\alpha$ -HER2. The data were successfully fitted using a sphere (DAB) model (time < 3.7 s) and a plate model (time > 3.7 s). The fitted curves are represented by the black curves. Plots of the (b) invariant  $Q$ , (c) mean particle size ( $R$  or  $T$  depending on the particle growth model), and (d) mean inter-particle distance ( $\langle d \rangle$ ) were calculated from the time-resolved SAXS patterns. It should be noted that the lateral dimension of the plates cannot be quantified as they are larger than the 100 nm resolution limit.

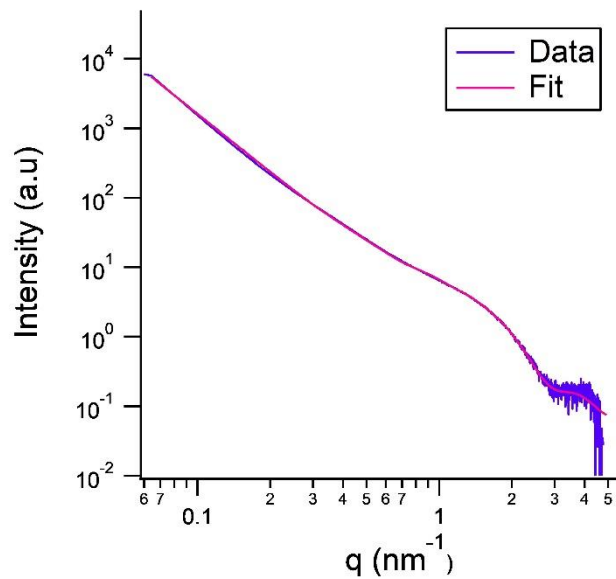


**Figure S9.** SAXS pattern of the dry powder of ZIF-C\* $\alpha$ -HER2 and fitted data. By fitting the SAXS pattern with a hierarchical sphere ScS model consisting of large aggregates and aggregated spherical pores (with a size distribution and an SHS structure factor), it is possible to identify the presence of cavities in the particles. Cavities with an average size of 3 nm and an average distance of 13.4 nm between the cavities were measured. These cavities correspond to the Fc fragments of the Ab that are embedded in the MOF particles.

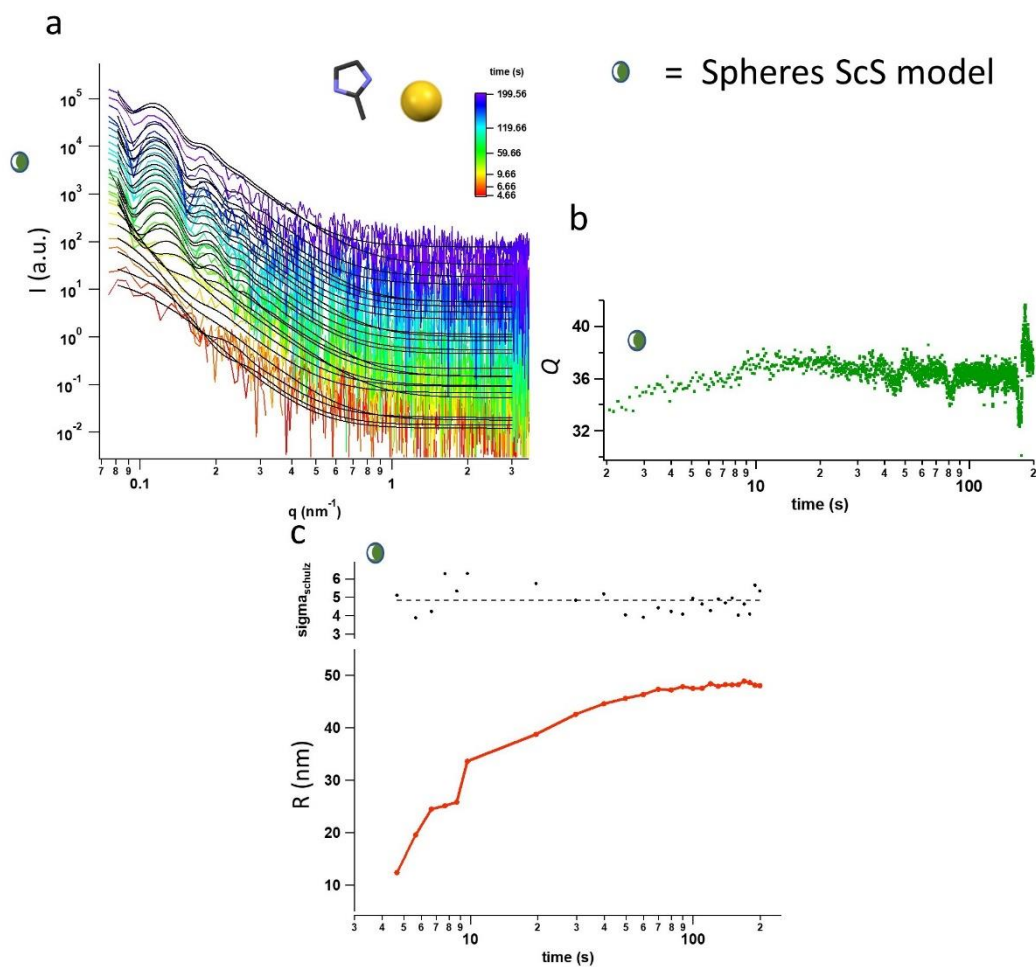


**Figure S10.** (a) Time-resolved SAXS patterns of the growth of bare MOF (no Ab or Ab components were mixed with the ligand solution). The data were successfully fitted with the spheres ScS model. The fitted curves are represented by the black curves. Plots of the (b) invariant  $Q$  and (c) mean sphere radius ( $R$ , and parameter  $\sigma$  of the Shultz model) were calculated from the time-resolved SAXS patterns.

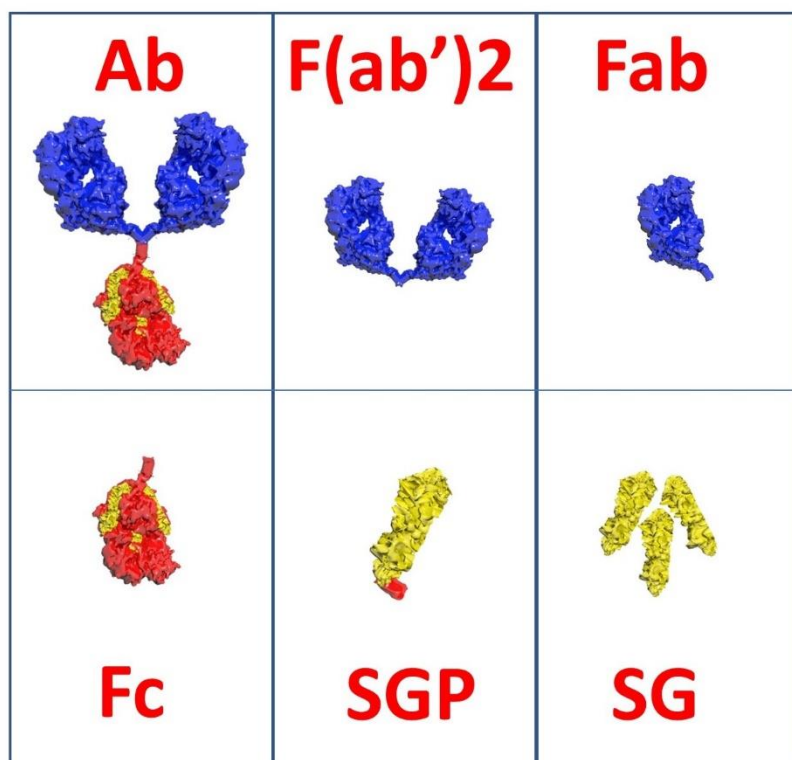


**Figure S11.** Schematic representations of the different Ab components that were investigated using time-resolved SAXS.

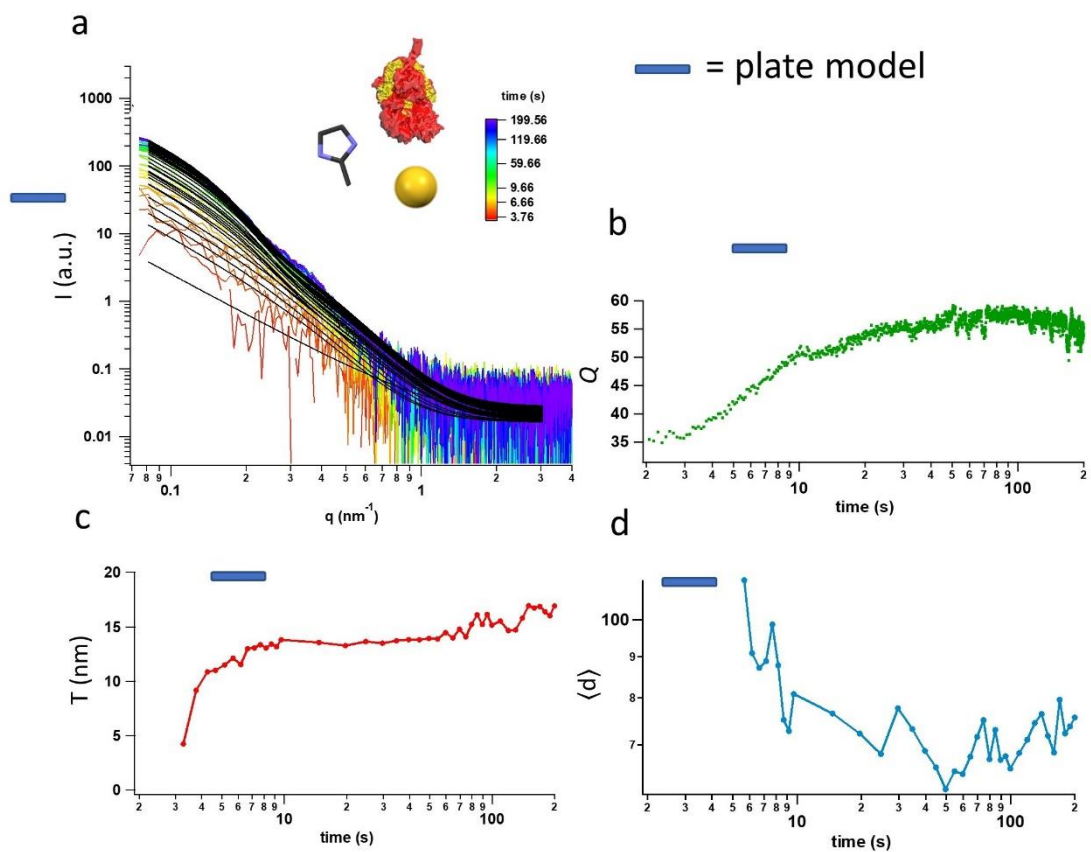


**Figure S12.** (a) Time-resolved SAXS patterns of the growth of ZIF-C in the presence of the Fc region. The data were successfully fitted using the plate model. The fitted curves are represented by the black curves. Plots of the (b) invariant  $Q$ , (c) mean particle size ( $T$ , calculated for time  $> 3.7$  s), and (d) mean inter-particle distance ( $\langle d \rangle$ ) calculated from the time-resolved SAXS patterns. The calculated average thickness of the plates was  $16 \pm 1$  nm. The calculated mean inter-particle distance was calculated after 5 s (the first experimental point that can be associated to a structure factor).

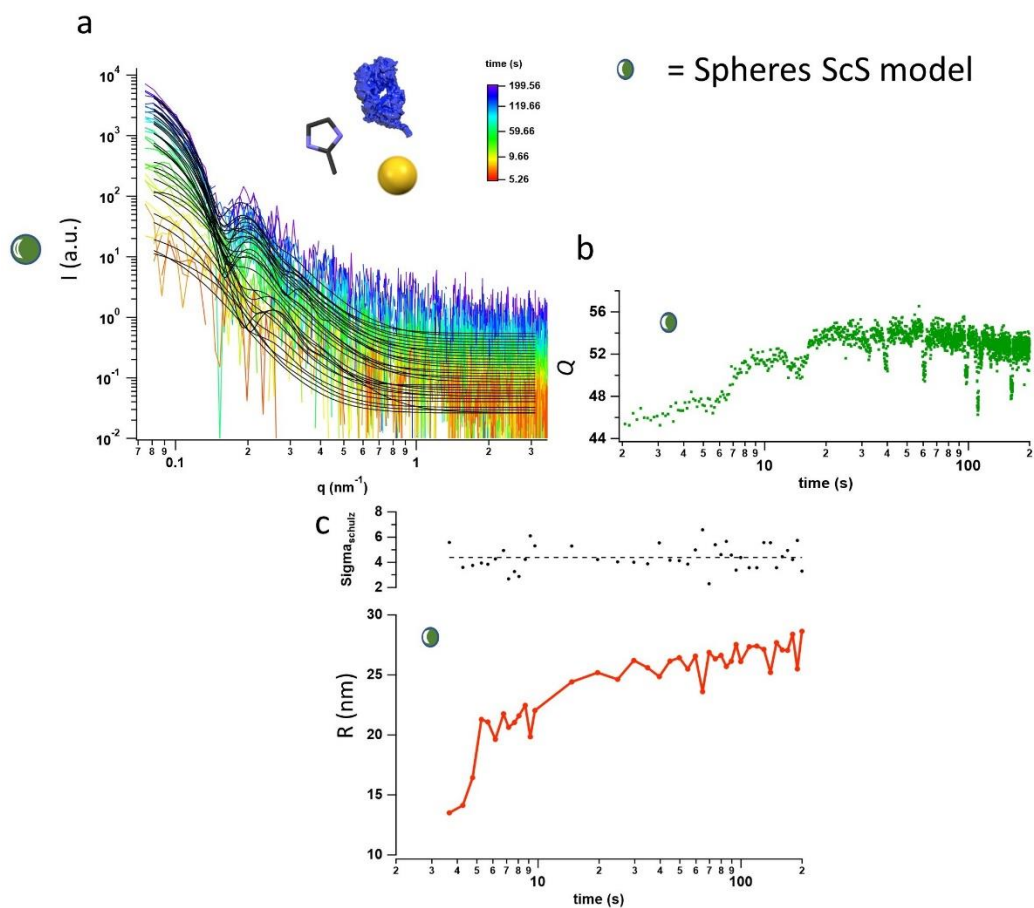


**Figure S13.** (a) Time-resolved SAXS patterns of the growth of ZIF-C in the presence of the Fab region. The data were successfully fitted with the spheres ScS model. The fitted curves are represented by the black curves. Plots of the (b) invariant  $Q$  and (c) mean sphere radius ( $R$ , and parameter  $\sigma$  of the Shultz model) were calculated from the time-resolved SAXS patterns.

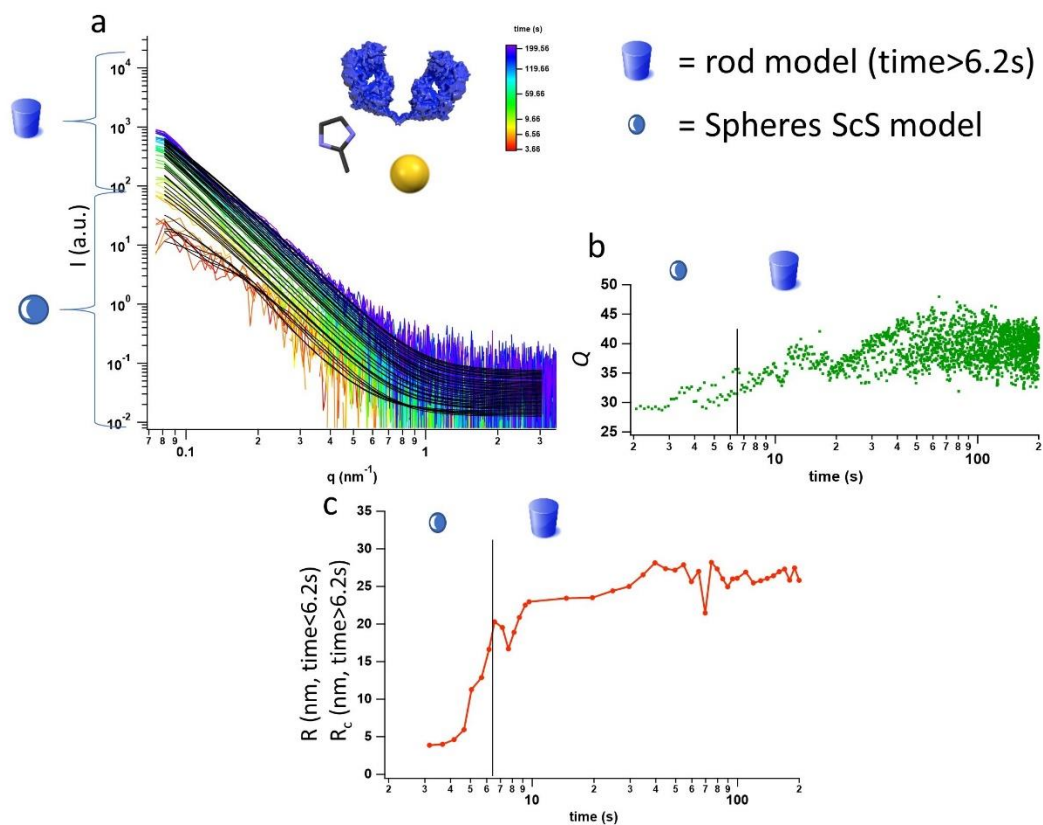


**Figure S14.** (a) Time-resolved SAXS patterns of the growth of ZIF-C in the presence of the F(ab')<sub>2</sub> region. The data were successfully fitted using the spheres ScS model combined with the structure factor  $S_{\text{SHS}}(q)$  (time < 6.2 s) and the rod model (time > 6.2 s). The fitted curves are represented by the black curves. Plots of the (b) invariant  $Q$  and (c) mean particle size ( $R$  (spheres) or  $R_c$  (rods)) were calculated from the time-resolved SAXS patterns.

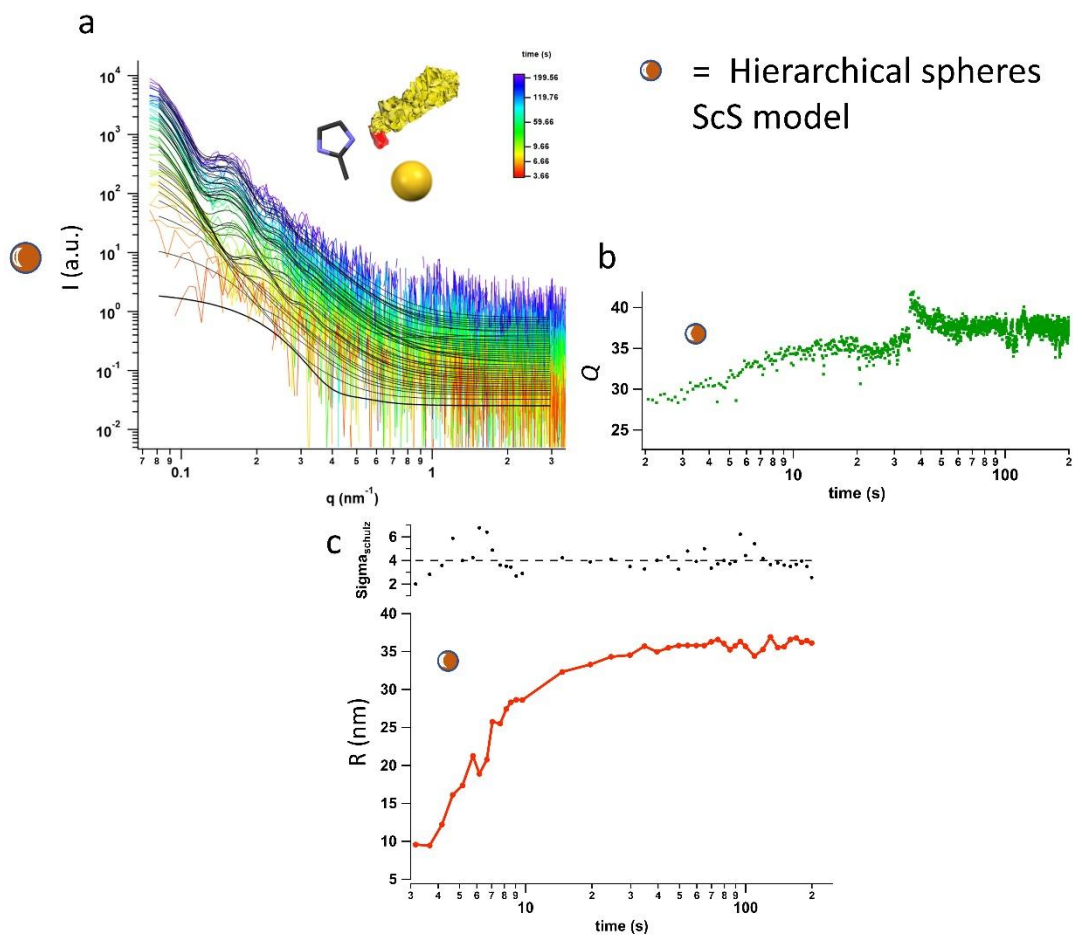


**Figure S15.** (a) Time-resolved SAXS patterns of the growth of ZIF-C in the presence of SGP. The data were successfully fitted using the hierarchical spheres ScS model. The fitted curves are represented by the black curves. Plots of the (b) invariant  $Q$  and (c) mean sphere radius ( $R$ , and parameter  $\sigma$  of the Shultz model) were calculated from the time-resolved SAXS patterns.

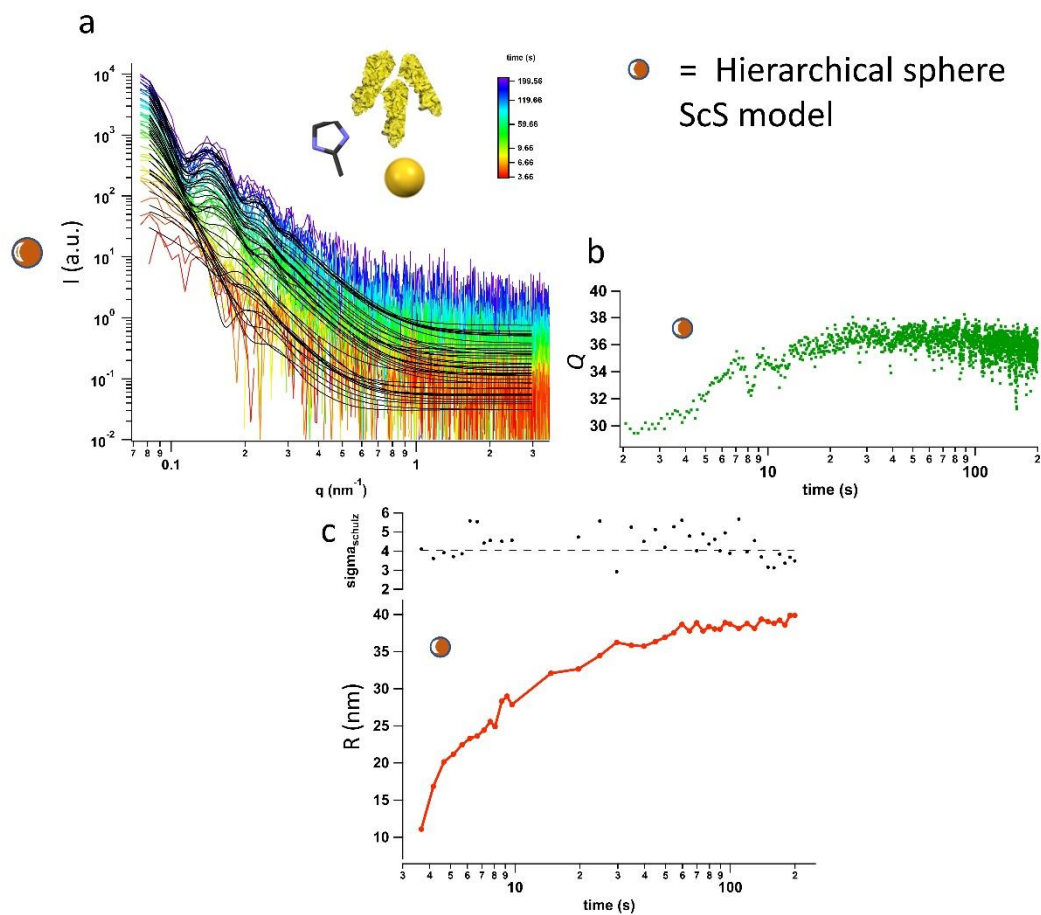


**Figure S16.** (a) Time-resolved SAXS patterns of the growth of ZIF-C in the presence of SG. The data were successfully fitted using the hierarchical spheres ScS model. The fitted curves are represented by the black curves. Plots of the (b) invariant  $Q$  and (c) mean sphere radius ( $R$ , and parameter  $\sigma$  of the Shultz model) were calculated from the time-resolved SAXS patterns.

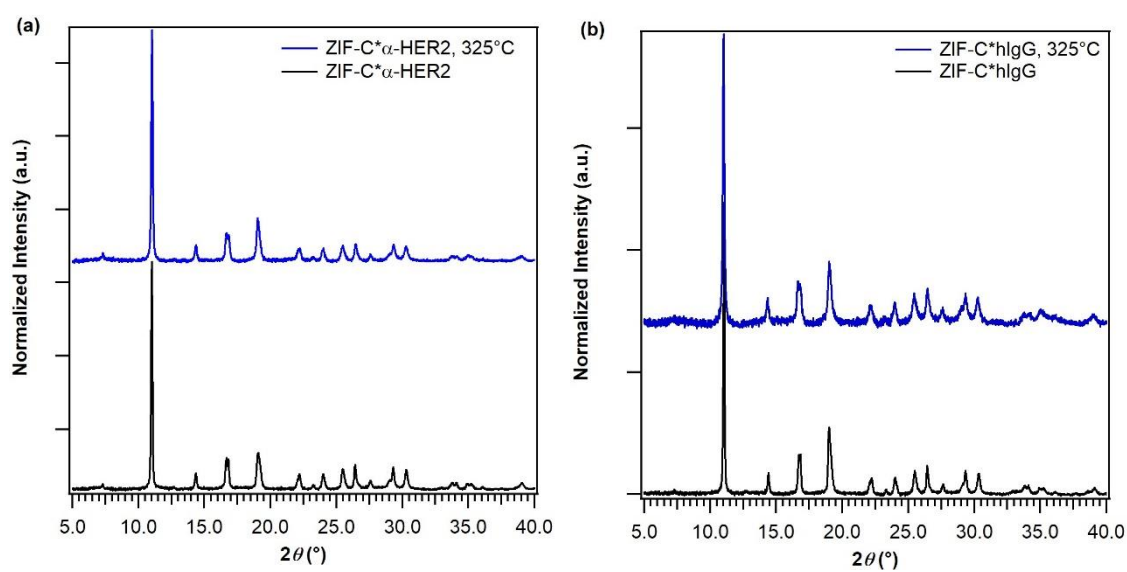


**Figure S17.** XRD patterns of (a) ZIF-C\* $\alpha$ -HER2 and (b) ZIF-C\*hIgG before and after pyrolysis at 325 °C.

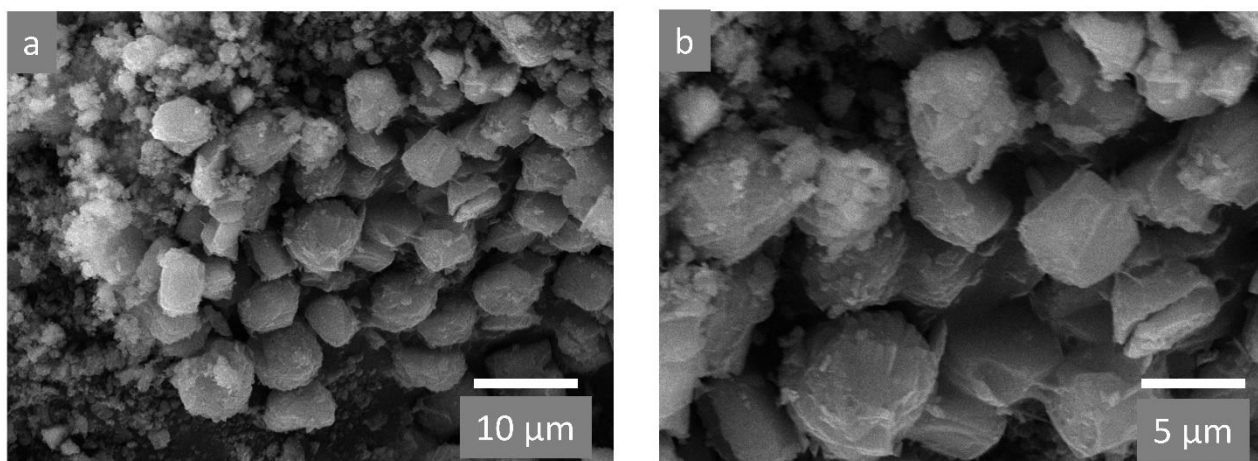


**Figure S18.** SEM images of ZIF-C\* $\alpha$ -HER2 after pyrolysis at 325 °C at different magnifications.

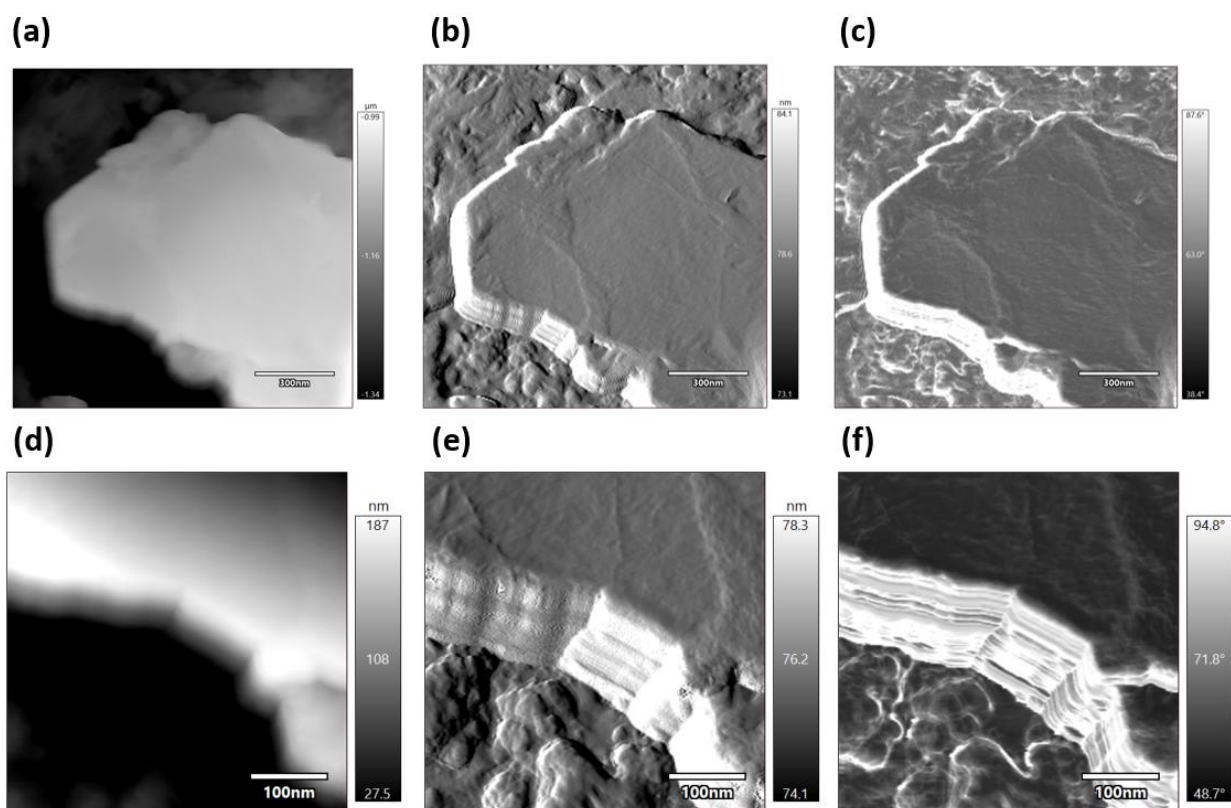


**Figure S19.** AFM (a, d) topography, (b, e) amplitude, and (c, f) phase contrast images of pyrolyzed ZIF-C\* $\alpha$ -HER2 showing a plate-like morphology. Images (d–f) show a high magnification of the edge of the structure.

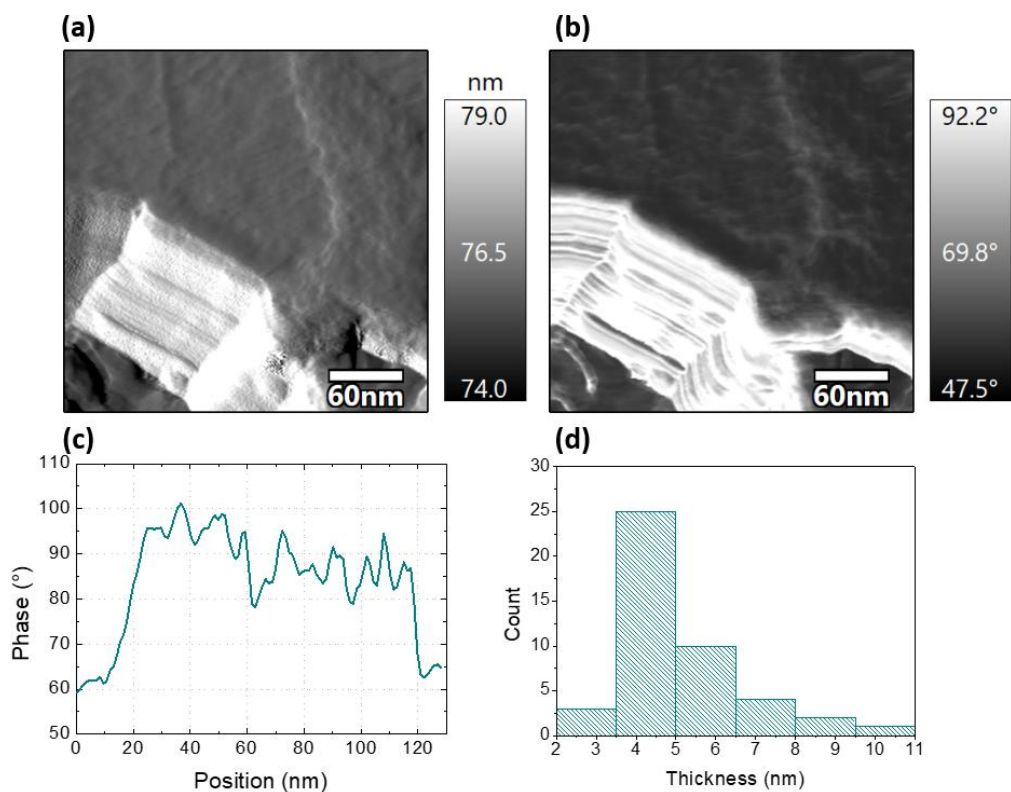


**Figure S20.** AFM analysis of pyrolyzed ZIF-C\* $\alpha$ -HER2 showing (a) amplitude and (b) phase images of the edge of the layered structure. (c) Typical line profile obtained from the phase image. (d) Histogram of the layer thickness populated from several line profiles obtained from different sample regions. The plate thickness typically ranged from 3 to 5 nm. Higher values were observed that could be attributed to multiple layers that were not resolved by the AFM measurement. Lateral resolution in these images is 1.2 nm (lateral sizes may be overestimated owing to convolution with the AFM tip).

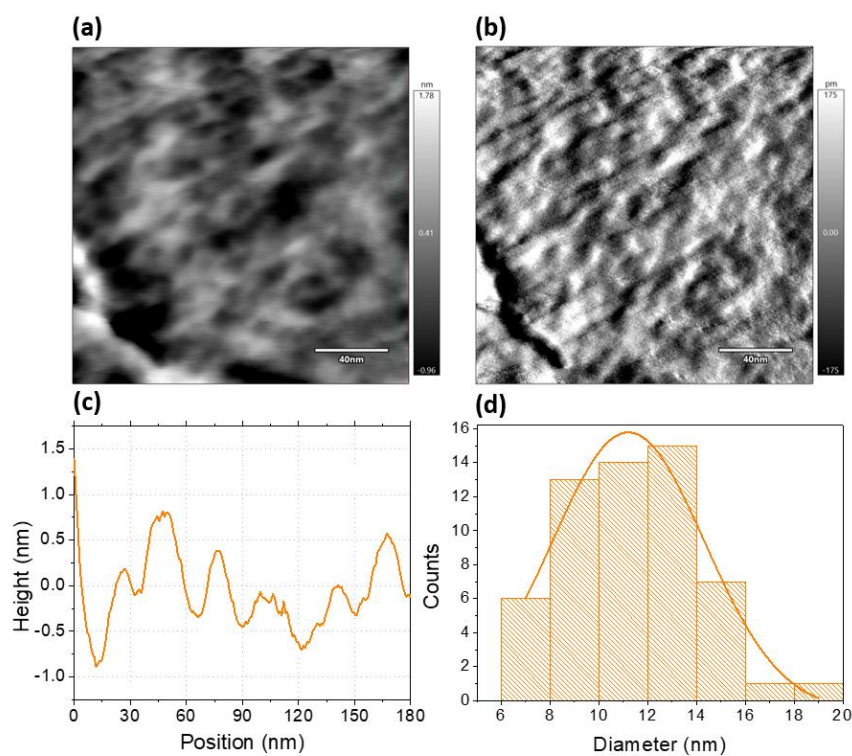


**Figure S21.** AFM analysis of pyrolyzed ZIF-C\* $\alpha$ -HER2 showing (a) topography and (b) amplitude images of a region on the surface of the plates shown in Figure S19. (c) Typical line profile obtained from topography analysis in (a) showing the cavities on the surface. (d) Histogram of the cavity diameter values obtained from different line profiles obtained from different sample regions and a corresponding Gaussian distribution fit. The calculated cavity diameter value was  $11 \pm 3$  nm (center and standard deviation value).

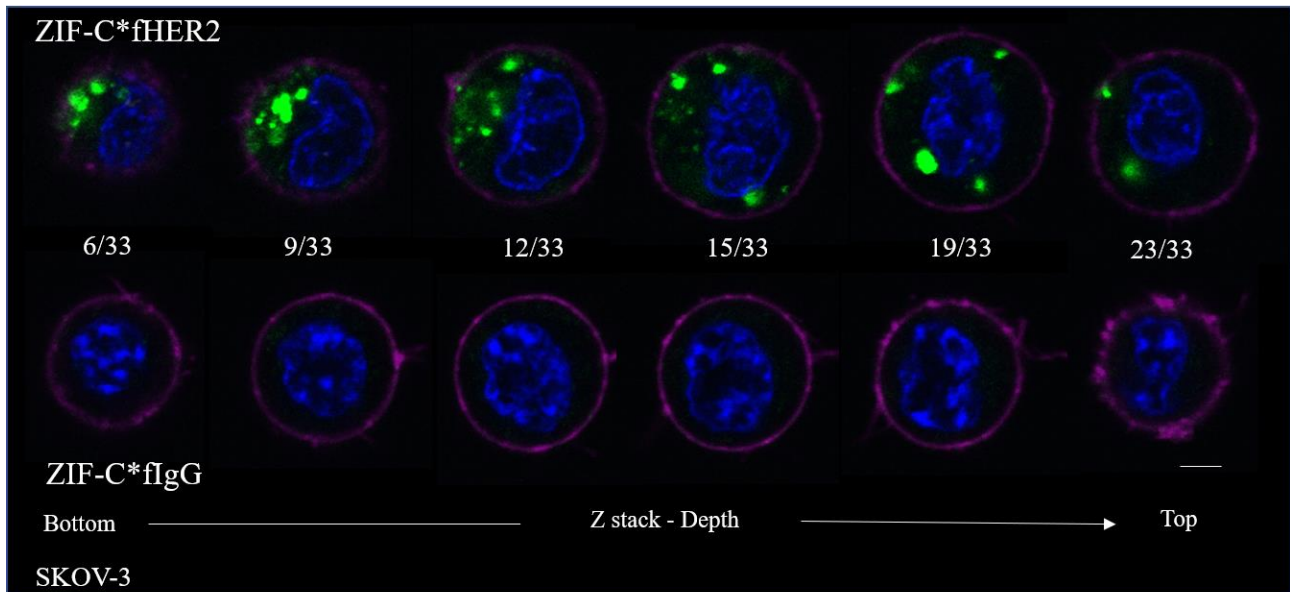


**Figure S22:** Cellular internalization of ZIF-C\* $\alpha$ -fHER2, representative confocal fluorescence microscopy Z stack images of SKOV-3 cells after 30 min incubation at 37 °C with either ZIF-C\*fHER2 (top row) or ZIF-C\*fIgG (bottom row). Z stack images were acquired from the bottom to the top of the cells. Nuclei are stained with 4',6-diamidino-2-phenylindole (blue) and cell membrane with Wheat Germ Agglutinin, Alexa Fluor™ 647 (pink). Scale bar, 5  $\mu$ m. Slice numbers (1-33) indicate the image position within Z stack of the cell.

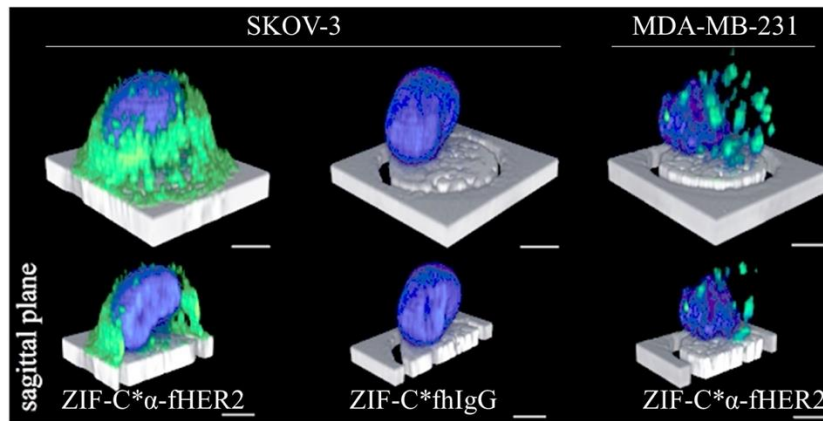


**Figure S23:** 3D confocal microscopy images of ZIF-C\*fAb internalization (Ab =  $\alpha$ -fHER2 or fhIgG). SKOV-3 (HER2-R+) or MDA-MB-231 (HER2-R-) cells were incubated with either ZIF-C\*  $\alpha$ -fHER2 (green) or ZIF-C\*fhIgG (green) and DAPI DNA stain (blue).

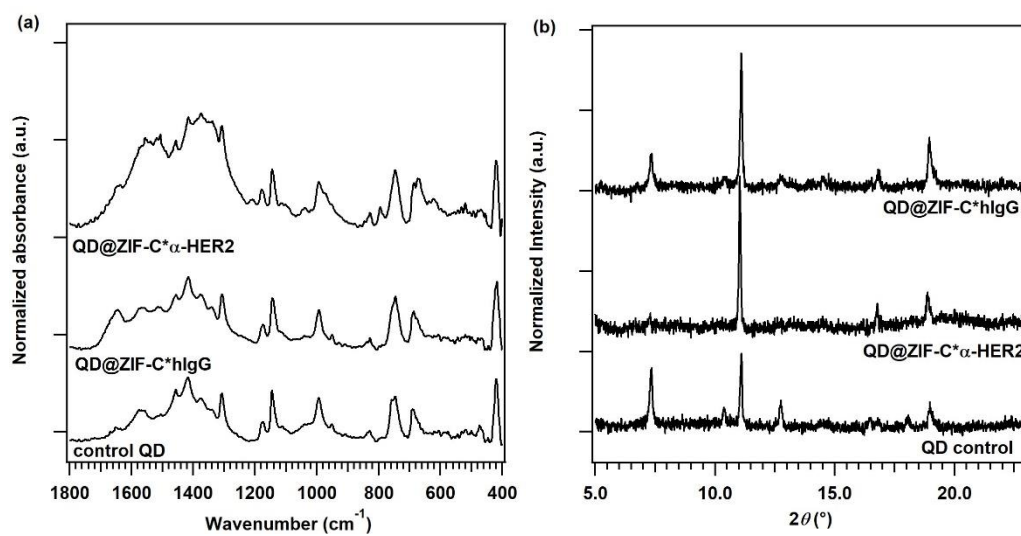


**Figure S24.** (a) FTIR spectra and (b) XRD patterns of QD@ZIF-C\*α-HER2, QD@ZIF-C\*hIgG, and MOF grown in the presence of QDs only as a control experiment (control QD).

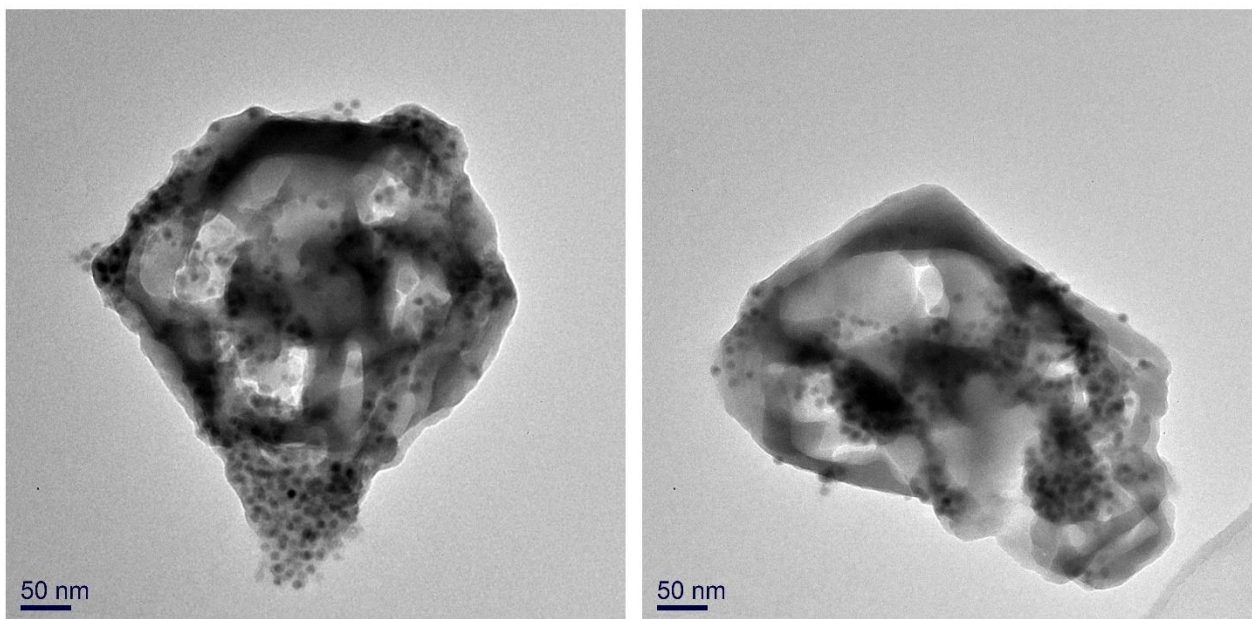


**Figure S25.** TEM images of QD@ZIF-C\* $\alpha$ -HER2.

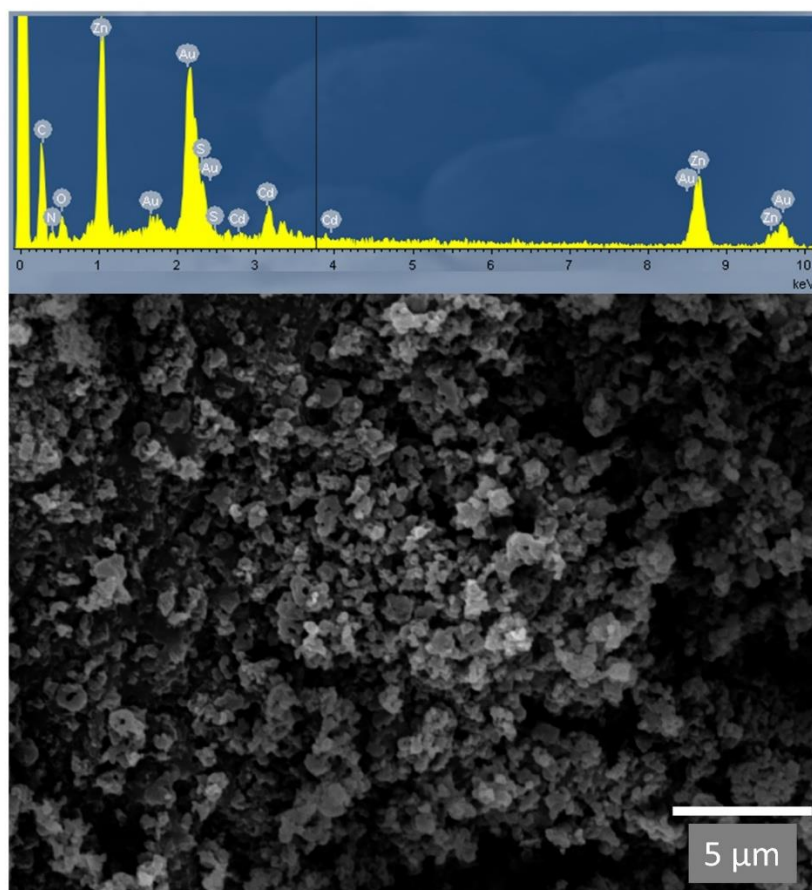


**Figure S26.** SEM image and a representative EDX spectrum (collected from a  $0.5 \times 0.5 \mu\text{m}^2$  region) of QD@ZIF-C\* $\alpha$ -HER2.

## References

- [1] J. Schindelin, I. Arganda-Carreras, E. Frise, V. Kaynig, M. Longair, T. Pietzsch, S. Preibisch, C. Rueden, S. Saalfeld, B. Schmid, J.-Y. Tinevez, D. J. White, V. Hartenstein, K. Eliceiri, P. Tomancak, A. Cardona, *Nat Methods* **2012**, *9*, 676.
- [2] H. Amenitsch, M. Rappolt, M. Kriechbaum, H. Mio, P. Laggner, S. Bernstorff, *J Synchrotron Radiat* **1998**, *5*, 506.
- [3] G. Porod, O. Glatter, O. Kratky, *Small Angle X-Ray Scattering* (Eds.: O. Glatter, O. Kratky), Academic Press, London, **1982**, 22.
- [4] R. V. Sharma, K. C. Sharma, *Phys Statistical Mech Appl* **1977**, *89*, 213.
- [5] D. Pontoni, S. Finet, T. Narayanan, A. R. Rennie, *J Chem Phys* **2003**, *119*, 6157.
- [6] S. Förster, A. Timmann, M. Konrad, C. Schellbach, A. Meyer, S. S. Funari, P. Mulvaney, R. Knott, *J Phys Chem B* **2005**, *109*, 1347.
- [7] P. Debye, H. R. Anderson, H. Brumberger, *J Appl Phys* **1957**, *28*, 679.
- [8] M. Kotlarchyk, S. Chen, *J Chem Phys* **1983**, *79*, 2461.
- [9] M. Kotlarchyk, R. B. Stephens, J. S. Huang, *J Phys Chem* **1988**, *92*, 1533.